Chemical Compositions Of Red Giant Stars in the Old Open Cluster NGC 7789

Neel Nagarajan[1] , Christopher Sneden[1] , Melike Afşar[2] , and Catherine A. Pilachowski[3]

[1] Department of Astronomy and McDonald Observatory, The University of Texas, Austin, TX 78712, USA; neelnagarajan@utexas.edu, chris@verdi.as.utexas.edu
[2] Department of Astronomy and Space Sciences, Ege University, 35100 Bornova, İzmir, Turkey; melike.afsar@gmail.com
[3] Department of Astronomy, Indiana University, Bloomington, IN 47405, USA; cpilacho@indiana.edu

Abstract

We have gathered optical-region spectra, derived model atmosphere parameters, and computed elemental abundances for 15 red giant stars in the open cluster NGC 7789. We focus on the light element group CNOLi that provides clues to evolutionary changes associated with internal fusion events and chemical mixing. We confirm and extend an early report that NGC 7789 stars 193 and 301 have anomalously large Li abundances, and that these values are apparently unconnected to any other elements' abundances in these stars. A companion study of He I λ10830 lines in both field stars and cluster members shows that star 301 has a strong He feature while star 193 does not. Possible explanations for the large Li abundances of these stars include helium flash-induced mixing events and binary interactions at some past or present times. In either case an internal eruption of energy could cause fresh synthesis of lithium via the Cameron-Fowler Berillyum transport mechanism. Rapid transport of lithium to the outer layers may have created significant chromospheric transient disturbances, producing enough helium ionization to allow for the strong λ10830 absorption in star 301.

Unified Astronomy Thesaurus concepts: High resolution spectroscopy (2096); Stellar atmospheres (1584); Chemically peculiar giant stars (1201); Open star clusters (1160)

Supporting material: machine-readable table

1. Introduction

Red giant stars typically exhibit low lithium abundances relative to those of main-sequence stars. During main-sequence stars' lives, Li is easily destroyed in high temperature interior regions as part of the proton-proton cycle of hydrogen fusion: $^7\text{Li}(p, \alpha) \rightarrow {}^4\text{He}$. As main-sequence stars evolve to become subgiants and then red giants, their deepening convective envelopes mix surface and interior layers, effectively cleaning the stellar atmospheres of their natal Li contents.

Because of this lithium-depletion process we typically observe surface Li abundances to be large in main-sequence stars (as much as $\log \epsilon(\text{Li}) \sim 3.3$)[4] but much lower in red giant stars ($\log \epsilon(\text{Li}) \lesssim 1.5$). However, around one percent of red giant stars in our Galaxy have unusually high Li abundances, as evidenced by a strong Li λ6707 absorption. Many papers have reported discoveries of Li-rich giants. Lithium excess is defined in various ways, but most papers suggest that red giants have anomously large Li abundances if $\log \epsilon(\text{Li}) \gtrsim 1.5$.

Two main sources have been suggested for such Li overabundances in red giants. First, it might be possible for Li to be added as an expanding stellar envelope engulfs a companion, typically thought to be a terrestrial companion (e.g., Alexander 1967). Second, fresh Li could be produced in the interiors of a star in the so-called beryllium transport mechanisim (Cameron & Fowler 1971), in which Li is

synthesized via $^3\text{He}(\alpha, \gamma)^7\text{Be}(e^-,\nu)^7\text{Li}$ and then dredge up to the surface before it can be destroyed in normal pp-chain hydrogen fusion. The assets and liabilities of these ideas are discussed in more detail in many papers, e.g., Casey et al. (2019), Deepak & Reddy (2019), and Martell et al. (2021). Recently, Sneden et al. (2022; hereafter Paper I) conducted a large survey of He I 10830 Å chromospheric lines, discovering a correlation between high Li abundances and very large λ10830 absorption strengths. Apparently the generation of Li in red giant envelopes is often accompanied by major disturbances in their outer atmospheres.

Some recent studies have begun to search for Li-rich stars in open clusters, where masses and ages can be estimated; e.g., Anthony-Twarog et al. (2013), Carlberg et al. (2016), Magrini et al. (2021), and Sun et al. (2022). In the present work we revisit the intermediate age open star cluster NGC 7789, which contains the first two red giants reported to have anomalously large Li abundances ($\log \epsilon(\text{Li}) \sim +2.4$; Pilachowski 1986). This cluster is relatively bright and has an extensive literature history. At age 1.5 Gyr (Gao 2018) NGC 7789 has a well-developed red giant branch, and has been subjected to several high-resolution spectroscopic analyses, but apparently without focus on its Li abundance anomaly since the Pilachowski study. Basic data for NGC 7789 are summarized in Table 1.

Pilachowski (1986) reported significant Li abundance excesses in NGC 7789 193 and NGC 7789 301 (hereafter labeled stars 193 and 301). Paper I included these stars and eight other cluster members from the Pilachowski (1986) sample. However, the optical spectra from the paper over 3 decades ago were of modest spectral resolution and signal-to-noise ratio (S/N); these stars lack recent accessible optical high-resolution spectra in the Li I λ6707 region. Therefore we have gathered and analyzed new optical echelle spectra for these NGC 7789 stars. In this paper we report Li abundances and discuss the Li-He connection for NGC 7789 red giants.

---

[4] We adopt the standard spectroscopic notation (Wallerstein & Helfer 1959) that for elements A and B, $[\text{A/B}] \equiv \log_{10}(N_\text{A}/N_\text{B})_\star - \log_{10}(N_\text{A}/N_\text{B})_\odot$. We use the definition $\log \epsilon(\text{A}) \equiv \log_{10}(N_\text{A}/N_\text{H}) + 12.0$, and equate metallicity with the stellar [Fe/H] value.

Table 1
Basic Data for NGC 7789

Quantity	Value[a]
R.A.	23:57:24
Decl.	+56:42:30
l (Galactic)	115°53
b (Galactic)	−5°53
Parallax	0.45 mas
Distance	2337 pc
Reddening	0.28 mag
Distance Modulus	11.72
Age	1.5 Gyr
μ (R.A.)	−0.92 mas
μ (Decl.)	−1.93 mas
Radial Velocity	−54.5 km s^{-1}

Note.
[a] From WEBDA or SIMBAD except in the case of the Reddening and the age (age is from Gao 2018). For the reddening, we used the value found in (Jacobson et al. 2011) and Overbeek et al. (2015), quoting Gim et al. (1998) and Tautvaišienė et al. (2005).

In Section 2 we describe the stellar sample, our observations, and the reduction steps to produce the final spectra. The model atmosphere and abundance analyses are outlined in Section 3. We discuss the results in Section 4 with particular emphasis on the LiCNO abundance group and relation to the $\lambda 10830$ data from Paper 1, and summarize our conclusions in Section 5.

2. Observations and Reductions

2.1. The Stellar Sample

We observed and analyzed 15 NGC 7789 red giants. The program stars are listed in Table 2 along with their astrometric and photometric properties of interest to our work. Inspection of the parallax and proper motion data in this table reveals that star 193 is discordant and likely not a member of NGC 7789. The possibility that star 193 is a nonmember arose in Pilachowski (1986), but the star was not discarded because its high Li abundance would make the star interesting regardless of its membership status. We also retained star 193 in our work, and will comment on it later.

We began with a cluster membership analysis. We considered stars in a search radius roughly double the radius of the WEBDA cluster chart for NGC 7789. We gathered the astrometric data for stars in this area from the GAIA (Gaia Collaboration et al. 2016) data archive Gaia Collaboration et al. (2022). We retained stars with GAIA parameters parallax p and proper motions $\mu_{R.A.}$, $\mu_{decl.}$ in the following ranges respectively: 0.4 to 0.5, −1.2 to −0.6, and −2.3 to −1.65. All these ranges are centered on the cluster mean values as presented in SIMBAD.

After elimination of nonmember stars, we then constructed an extinction-corrected Gaia-based color–magnitude diagram (CMD) for NGC 7789. We converted $E(B-V)$ from Table 1 to $E(BP-RP) = 0.39$ using two equations: $E(BP-RP) \simeq 4.507 EW_{862}$ (developed by Gaia collaboration et al. 2022), and $E(B-V) \simeq 3.1 EW_{862}$ (from Table 3 of Gaia collaboration et al. 2022). Here, EW_{862} is the equivalent width of the diffuse interstellar band at 862 nm and $E(B-V) \simeq 3.1 EW_{862}$ is a relationship between the band strength and the UBV standard reddening value.

We converted the total extinction to Gaia units via the relation $A_G/A_V \simeq 0.95$ from Jordi et al. (2010). Application of these formulae yielded the $(BP-RP)_0$ and M_{G0} values employed to create the CMD shown in Figure 1. This is similar to other CMDs for NGC 7789 in the literature, e.g., Overbeek et al. (2015), Gao (2018), and Cantat-Gaudin et al. (2018). We have included star 193 in this plot even though it is not a probable NGC 7789 member, and we have arbitrarily used the cluster reddening values in placing it in the figure. Its position in Figure 1 should not be used to infer its evolutionary history. Furthermore, star 765's membership may also be in question due to it is relatively low parallax (Table 2), but its proper motions are consistent with NGC 7789 membership. The dereddened CMD presented in Figure of Sandquist et al. (2020) for multiple open clusters shows that the approximate red clump center is at $[(BP-RP), M_{G0}] = [1.1, 0.4]$, which is essentially coincident to the red clump center for NGC 7789.

In Figure 1 the stars with $(BP-RP)_0 \lesssim 0.4$ are easily identified as blue straggler stars (BSS). Such members of NGC 7789 have been known for many decades since the pioneering CMD study of Burbidge & Sandage (1958). Blue stragglers probably result from mass transfer in binary or triple systems (e.g., McCrea 1964; Hills & Day 1976; Perets & Fabrycky 2009), suggesting that NGC 7789 has a relatively large set of present or past multiple star systems.

2.2. High-resolution Spectra

We gathered high-resolution spectra of the target stars with the McDonald Observatory 2.7 m Harlan J. Smith Telescope and Tull Echelle Spectrograph (Tull et al. 1995). The combination of slit, dispersing elements, and detector yielded spectral resolution of $R \equiv \lambda/\Delta\lambda \simeq 45,000$. The observed spectral range covered 3500−9500 Å. However, our red giants have sharply decreasing fluxes and substantial spectral line blanketing toward shorter wavelengths, so in consequence our analyses considered only wavelength regions with $\lambda > 5300$ Å. Typical S/Ns near 6000 Å were S/N ∼ 100 per resolution element. The obtained spectra included star 971, a red giant tip member of NGC 7789. This star is by far the reddest one of our sample (Table 2). Its low temperature along with inclement weather during observation resulted in a very noisy reduced spectrum, and so we dropped it from further consideration in this paper.

All spectra were obtained in a single observing run covering 7 nights. Total integration times for each program star were 2–3 hr, obtained in individual half-hour exposures. The program stars' observations were accompanied by bias, dark, flat-field incandescent, and Th-Ar lamp integrations. We also observed several rapidly rotating hot stars to facilitate cancellation of telluric features in the program stars.

2.3. Reductions and Equivalent Widths

We performed all spectral reductions using the IRAF[5] (Tody 1986, 1993) facility. The reduction tasks included bias subtraction, cosmic ray excision, echelle order extraction, continuum normalization, pixel to wavelength conversion, and velocity correction to rest wavelength scales.

One of the chief goals of our study is to investigate the relationship between Li abundance and He I $\lambda 10830$ absorption
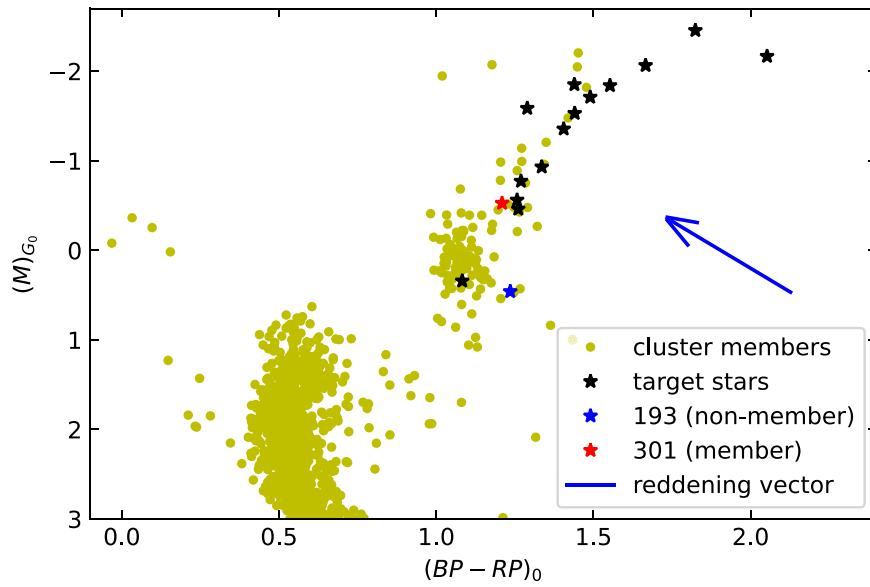
---

5 https://iraf-community.github.io

Figure 1. An extinction-corrected CMD for NGC 7789 using GAIA photometric data. As identified in the plot legend, the star-shaped symbols show the red giants of this study. The reddening vector shows the direction and length by which we shifted the stars on the CMD to correct for interstellar reddening effects.

Table 2
Basic Data for Target Stars[a]

Star[b]	parallax mas	μ (R.A.) mas	μ (decl.) mas	G	BP − RP	V	B − V
72	0.5040	−0.775	−2.071	10.22	2.06	11.05	1.74
193	0.6742	+8.491	−2.338	12.12	1.63	12.61	1.42
301	0.5144	−1.123	−2.444	11.72	1.60	12.27	1.34
329	0.4949	−0.883	−1.890	11.80	1.66	12.31	1.38
353	0.4855	−0.820	−2.017	12.10	1.65	12.59	⋯
461	0.4793	−0.968	−1.933	10.69	1.88	11.35	1.63
468	0.4829	−0.886	−1.914	10.53	1.83	11.61	1.14
494	0.4898	−0.825	−1.985	9.86	2.22	10.74	1.68
501	0.4749	−0.830	−2.037	10.51	1.95	11.26	1.71
637	0.4882	−0.983	−1.716	11.90	1.65	12.40	1.42
669	0.4830	−0.775	−2.071	10.85	1.83	11.46	1.58
765	0.4175	−1.065	−2.033	11.11	1.68	11.59	1.21
970	0.4800	−0.970	−2.110	11.29	1.80	11.89	⋯
971	0.5398	−1.029	−2.105	9.97		11.05	1.90
1066	0.4867	−0.979	−2.055	11.43	1.73	11.99	⋯
1101	0.5004	−0.876	−2.013	12.65	1.48	13.05	⋯
$<\,>$[c]	0.4881	−0.919	−2.046				
σ[c]	0.0256	0.107	0.154				

Notes.
[a] Adopted from SIMBAD.
[b] Küstner (1923).
[c] Computed without star 193.

strength. In the left-hand panel of Figure 2 we show spectra of the Li I λ6707 resonance feature in all stars observed here, and in the right-hand panel we show the He I line in spectra collected for Paper 1.

We measured EWs of unblended atomic lines, beginning with the line lists used by Böcek Topcu et al. (2015) for their study of open cluster NGC 752 and by Böcek Topcu et al. (2016) for NGC 6940. We calculated the EWs with the SPECTRE[6] spectrum analysis code (Fitzpatrick & Sneden 1987). The line profiles were usually modeled by Gaussian functions, with occasional Voigt functions for the strongest lines. EWs could not be reliably measured for some lines below 5300 Å due to sharply decreasing fluxes and substantial spectral line blanketing; those lines were excluded from our analyses. The EWs are listed in Table 3.

3. Abundance Analyses

In this section we describe the steps in analyses that led to final abundances of elements in our NGC 7789 program stars. Our focus is on model atmospheric parameters and abundances of the LiCNO element group.

---

[6] https://www.as.utexas.edu/~chris/spectre.html

Table 3
Equivalent Widths

Species	λ	χ	$\log(gf)$	72	193	301	329	353	461	468	494	501	637	669	765	978	1066	1101
Na I	5682.64	2.101	−0.70	216	194	173	181	175	210	209	212	217	186	197	⋯	194	180	146
Na I	6154.23	2.101	−1.56	139	109	94	98	97	128	138	144	133	99	118	105	112	105	71
Na I	6160.75	2.103	−1.26	154	130	112	120	114	142	144	195	147	118	136	121	132	125	93
Mg I	5528.41	4.343	−0.62	290	321	275	266	261	299	290	291	⋯	236	285	⋯	272	279	209
Mg I	5711.08	4.343	−1.83	154	166	143	144	146	161	141	148	157	152	161	154	151	151	113
Mg I	7811.11	5.941	−0.95	99	143	80	79	81	94	⋯	101	93	86	91	85	81	92	⋯
Al I	6696.02	3.140	−1.35	140	212	99	131	123	163	121	150	126	102	148	101	109	130	72
Al I	6698.67	3.140	−1.64	90	88	54	76	66	91	88	99	88	74	86	73	78	75	41
Al I	7835.30	4.018	−0.65	111	125	85	81	74	103	93	117	109	79	98	81	97	85	64
Si I	5488.98	5.614	−1.90	29	54	33	44	42	33	36	25	31	46	40	31	41	41	34
Si I	5517.53	5.082	−2.61	22	35	33	27	23	32	⋯	35	⋯	36	34	31	⋯	28	25

Note. All EWs are in units of Å.

(This table is available in its entirety in machine-readable form.)

3.1. Model Atmospheres

We determined model atmospheric parameters and abundances from the line data information in the NGC 7789 spectra. Initially we attempted to use the measured EWs to estimate model parameters in a standard manner: (1) T_{eff}, from requiring low and high-excitation Fe I lines to yield the same Fe abundance on average; (2) $\log g$, from requiring abundance agreement between neutral and ionized lines of Fe and Ti; (3) V_{mic}, by forcing weak and strong Fe I lines to yield similar abundances; and (4) [M/H] by asking for stellar model metallicity to be consistent with derived abundances of most elements. We tried to follow the procedures outlined in Böcek Topcu et al. (2015, 2016) for NGC 752 and NGC 6940.

However, NGC 7789 red giant stars are substantially redder/cooler than those in the other two clusters, and its lines have significantly larger EWs. Unfortunately, almost all Fe I lines employed for the other clusters lie on the flat part of the curve-of-growth in NGC 7789 red giant stars. In general, the strongest Fe I lines have low excitation energies. The relative abundance insensitivity of these lines, combined with the line strength and excitation correlation makes it very difficult to determine V_{mic} and T_{eff} in the traditional manner.

Therefore we chose to derive T_{eff} values purely from atomic line depth ratios (LDRs). This method was pioneered by Gray & Johanson (1991) and involves identification of pairs of absorption lines whose strengths have very different responses to variations in T_{eff}. Gray & Johanson (1991) considered G-K stars, and concentrated on the 6200 Å spectral domain that has many low-excitation V I transitions that become much stronger with decreasing T_{eff}, usually pairing them with higher-excitation Fe I transitions that are much less sensitive to T_{eff} changes. The physical principles involved are basic Boltzmann/Saha relations that describe the populations of ionization/excitation states in stellar atmospheres (see extended discussions of these issues in Gray 2008). The work on LDRs has expanded to include other species in other spectral regions for stars in different temperature-gravity domains, e.g., Strassmeier & Schordan (2000) and López-Valdivia et al. (2019). Here we follow Böcek Topcu et al. (2015, 2016) in using the LDR calibrations of Biazzo et al. (2007), which are based on the original Gray & Johanson work.

With T_{eff} established the other parameters $\log g$, V_{mic}, and [M/H] were derived from line EWs as outlined above. In particular the microturbulent velocity was determined from forcing weak and strong Fe I lines to yield the same average abundances. The gravity was set exclusively through the requirement to force abundance agreement between these two Fe ionization states. We employed interpolated models from the ATLAS[7] grid (Kurucz 2011, 2018). To compute abundances we used the current version of the LTE plane-parallel line analysis code MOOG (Sneden 1973).[8] The derived atmospheric parameters are listed in Table 4, along with the abundances of Fe I and Fe II.

The Fe abundances were determined from on average 49 Fe I and 10 Fe II species. From these slightly subsolar values we set a uniform metallicity of [M/H] = −0.1. The mean metallicity for NGC 7789, <[Fe/H]> = −0.02 with $\sigma = 0.05$, is in reasonable accord with those determined in previous high-resolution spectroscopic studies: [Fe/H] = −0.04, $\sigma = 0.05$ (Tautvaišienė et al. 2005); [Fe/H] = +0.04, $\sigma = 0.07$ (Pancino et al. 2010); [Fe/H] = +0.02, $\sigma = 0.05$ (Jacobson et al. 2011); [Fe/H] = +0.03, $\sigma = 0.07$ (Overbeek et al. 2015).

Our study is not a comprehensive abundance survey of NGC 7789. It focuses mainly on the LiCNO element group and its relationship to He I $\lambda10830$ absorption strengths. We derived abundances from EWs of a few elements that have been featured in past studies. They are listed in Table 5 and in Figure 3 we compare some [X/Fe] values to those in previous papers. Our abundance uncertainties are larger than those reported in the comparison studies, but in most part they are in accord for Mg, Si, and Ca. The NGC 7789 abundances for Ti, Na, and Ni should be explored further in a study that concentrates on warmer, less line-rich stars than we have gathered for our work.

3.2. Lithium, Carbon, Nitrogen, and Oxygen

Light elements Li, C, N, and O may be altered during a star's lifetime through interior proton fusion reactions and envelope mixing. We derived abundances for these elements via matches of observed and synthetic spectra.

1. Lithium: nearly all Li abundances are derived from the Li I resonance doublet at 6707.8 Å, but in a small percentage of cool stars with very large Li abundances the excited-state transition at 6103.6 Å becomes

---

[7] Available at http://kurucz.harvard.edu/grids.html; model interpolation software was kindly provided by A. McWilliam and I. Ivans.
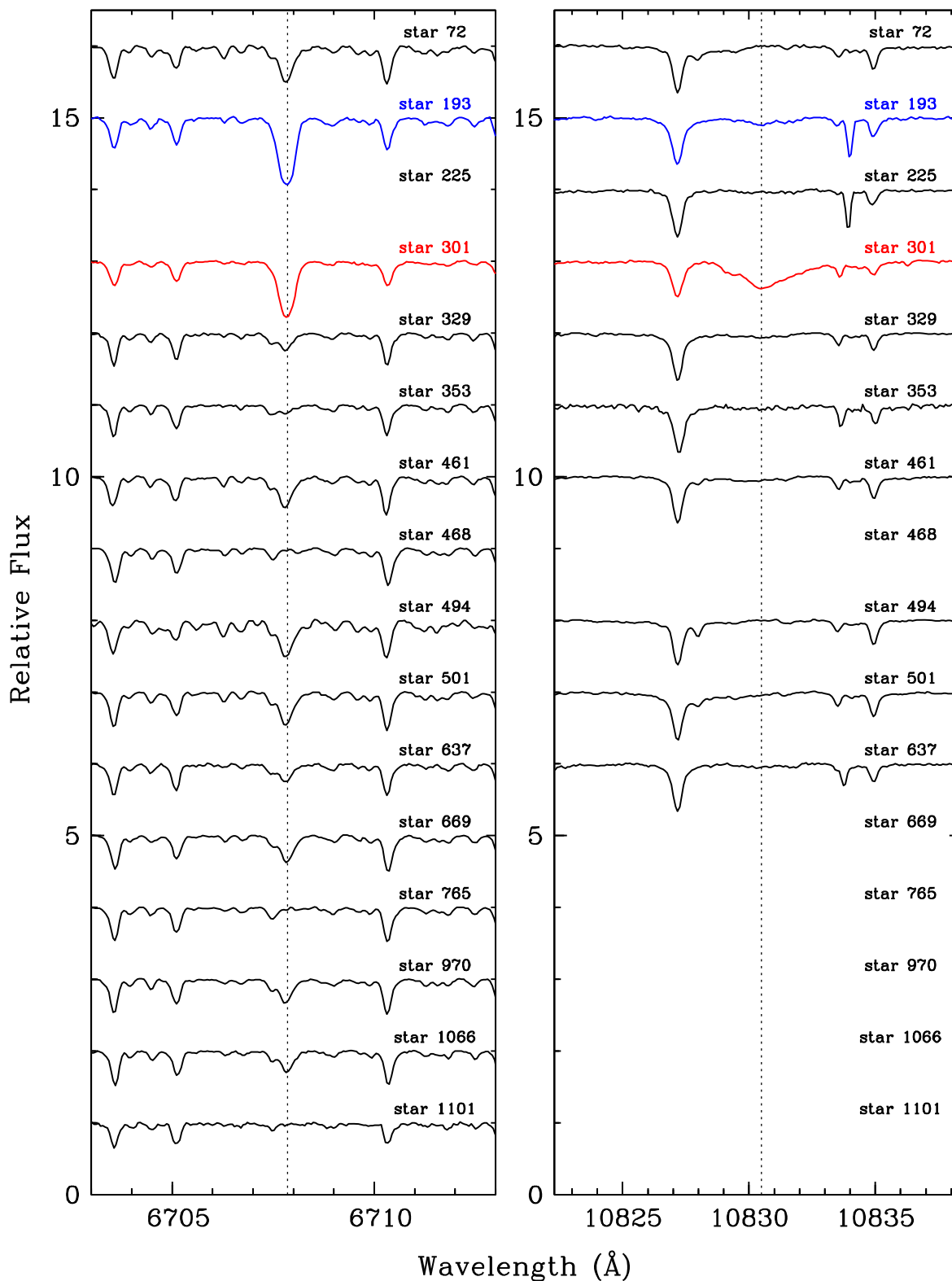[8] Available at http://www.as.utexas.edu/~chris/moog.html.

Figure 2. Spectra of the Li I $\lambda6707$ resonance transition in all NGC 7789 red giants observed with the Tull Spectrograph (left panel) and of the He I $\lambda10830$ transition in all of this cluster's stars observed with HET/HPF by Sneden et al. (2022; right panel). Attention is called to Li-rich stars 193 (in blue) and 301 (in red). All spectra of NGC 7789 giants observed with either instrument are shown in this figure.

detectable. We used both of these features in our analysis for stars 193 and 301.

2. Carbon: the best available spectral features for our stars were lines near the C_2 Swan system $(d^3\Pi_g - a^3\Pi_u)$ $(0-1)$ bandhead at 5635 Å. The stronger $(0-0)$ bandhead near

5165 Å is extremely crowded with other atomic and molecular features, and our spectra in the region of the comparable-strength $(1-0)$ bandhead, 4725 Å, are very noisy. Our spectra are even less reliable in the 4300 Å CH G-band wavelength domain. C I high-excitation lines can

Table 4
Model Atmosphere Parameters

Star	T_{eff} (K)	[M/H]	log g	V_{mic} km s^{-1}	[Fe/H] (I)	σ (I)	#lines (I)	[Fe/H] (II)	σ (II)	#lines (II)
72	4240	−0.1	2.00	1.00	0.01	0.18	50	0.01	0.26	12
193	4590	−0.1	2.50	1.60	−0.02	0.10	49	−0.02	0.16	12
301	4730	−0.1	2.60	1.55	−0.06	0.13	49	−0.07	0.17	11
329	4625	−0.1	2.40	1.40	0.04	0.12	52	−0.03	0.17	12
353	4675	−0.1	2.40	1.60	−0.13	0.12	50	−0.13	0.22	10
461	4315	−0.1	2.10	1.50	−0.01	0.15	48	−0.01	0.14	7
468	4370	−0.1	2.10	1.60	−0.05	0.14	44	−0.07	0.14	10
494	4170	−0.1	1.90	1.45	0.02	0.25[a]	49	0.02	0.19	9
501	4295	−0.1	2.10	1.50	0.00	0.15	46	0.00	0.11	7
637	4620	−0.1	2.60	1.50	−0.06	0.10	51	−0.06	0.08	9
669	4390	−0.1	2.00	1.45	−0.03	0.14	50	−0.02	0.33	10
765	4515	−0.1	2.30	1.40	0.07	0.15	50	0.06	0.12	10
970	4455	−0.1	2.30	1.55	−0.02	0.13	49	−0.02	0.08	9
1066	4530	−0.1	2.30	1.50	−0.03	0.13	53	−0.02	0.15	9
1101	5050	−0.1	2.65	1.40	−0.08	0.12	47	−0.08	0.13	7
$<>$					−0.02	0.14	49	−0.03	0.16	10
σ	225	…	0.24	0.07	0.05	0.04	…	0.05	0.07	…

Note.

[a] Star 494 had an exceptionally low S/N, which is why we ended up with an unusually large standard deviation. In addition, the reason there is such a wide range of standard deviations for Fe (II) is that many Fe (II) lines lay in noisy regions of our spectra, making them harder to measure and depending on the star.

Table 5
Output Abundances in Bracket ([X/Fe]) form

Star	Na	Mg	Al	Si	Ca	Sc2[a]	Ti1	Ti2	V[a]	Cr1	Cr2	Mn[a]	Fe1	Fe2	Ni	La[a]	Eu[a]
72	0.61	0.01	0.33	0.29	0.24	0.48	0.44	0.51	0.49	0.31	0.26	0.29	0.00	0.00	0.47	0.35	0.22
193	0.46	0.27	0.83	0.50	0.17	0.15	0.20	0.23	0.22	0.18	0.32	0.20	0.00	0.00	0.24	0.18	0.55
301	0.38	−0.03	0.12	0.20	0.32	0.13	0.20	0.33	0.20	0.31	0.23	0.05	0.00	0.00	0.12	0.24	0.17
329	0.45	−0.04	0.35	0.35	0.17	0.09	0.14	0.33	0.14	0.18	0.15	0.13	0.00	0.00	0.22	0.25	0.28
353	0.45	0.03	0.29	0.38	0.16	0.10	0.15	0.22	0.21	0.18	0.20	0.11	0.00	0.00	0.15	0.29	0.32
461	0.50	0.04	0.43	0.39	0.18	0.20	0.27	0.53	0.34	0.18	0.29	0.22	0.00	0.00	0.33	0.27	0.29
468	0.64	−0.13	0.22	0.42	0.20	0.16	0.28	0.16	0.32	0.15	0.07	0.21	0.00	0.00	0.35	0.37	0.48
494	0.77	0.01	0.43	0.39	0.18	0.11	0.47	0.69	0.58	0.30	0.53	0.12	0.00	0.00	0.46	0.36	0.19
501	0.57	0.19	0.26	0.29	0.18	0.16	0.33	0.41	0.41	0.33	0.20	0.13	0.00	0.00	0.35	0.38	0.46
637	0.41	−0.04	0.16	0.42	0.12	0.20	0.13	0.26	0.19	0.15	0.37	0.16	0.00	0.00	0.25	0.35	0.50
669	0.52	0.07	0.41	0.28	0.20	0.16	0.32	0.42	0.32	0.23	0.31	0.30	0.00	0.00	0.31	0.24	0.27
765	0.27	0.10	0.01	0.24	0.09	0.14	0.13	0.19	0.13	0.12	0.07	0.17	0.00	0.00	0.25	0.21	0.36
970	0.44	−0.07	0.16	0.40	0.12	0.13	0.14	0.29	0.21	0.10	0.17	0.15	0.00	0.00	0.25	0.31	0.35
1066	0.41	0.02	0.27	0.38	0.19	0.10	0.13	0.45	0.15	0.15	0.12	0.00	0.00	0.00	0.24	0.25	0.26
1101	0.43	0.03	0.06	0.19	0.05	−0.07	0.07	−0.03	0.04	0.02	−0.21	−0.07	0.00	0.00	0.05	0.21	0.45

Note.

[a] For these five elements, the abundances presented were found using the "blends" task instead of "abfind" due to the presence of hyperfine splitting. All other abundances were found using "abfind."

be detected but are not reliable abundance indicators for NGC 7789 cool giants.

3. Nitrogen: CN $A^2\Pi - X^2\Sigma^+$ red system lines can be detected in all wavelength regions beyond 6000 Å. We concentrated on strong (2−0) band features near 8000 Å to derive N abundances and $^{12}C/^{13}C$ ratios.

4. The [O I] $\lambda 6300$ ground-state line is the single reliable O abundance indicator in our spectra. Care must be taken with this transition since it is beset with blending by Ni I and CN contaminants, and can potentially be compromised by telluric O_2 absorption and night-sky [O I] emission.

To create atomic/molecular line lists for the synthetic spectrum calculations we used the linemake facility (Placco et al. 2021).[9] The code creates lists of transitions starting with the Kurucz (2011, 2018)[10] line compendium, and updating them with transition data from recent laboratory studies mainly by the Wisconsin–Madison atomic physics group (Den Hartog et al. 2021 and references therein) and by the Old Dominion University molecular physics group (e.g., Brooke et al. 2016 and references therein).

---

[9] https://github.com/vmplacco/linemake
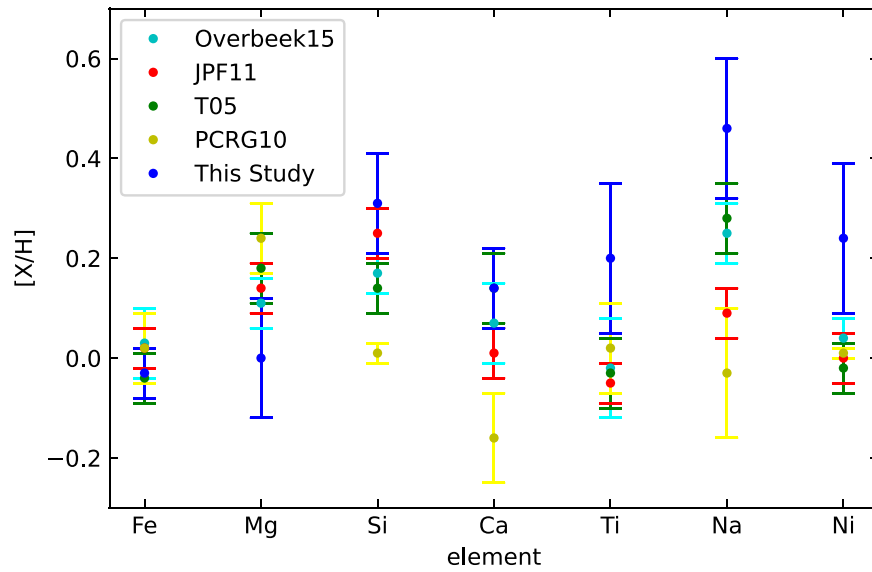[10] http://kurucz.harvard.edu/linelists.html

Figure 3. Comparison of NGC 7789 abundances in this paper to results from some previous papers. The various studies are identified by color types, as defined in the plot legend and are as follows: Overbeek et al. (2015), Jacobson et al. (2011), Pancino et al. (2010), and Tautvaišienė et al. (2005)
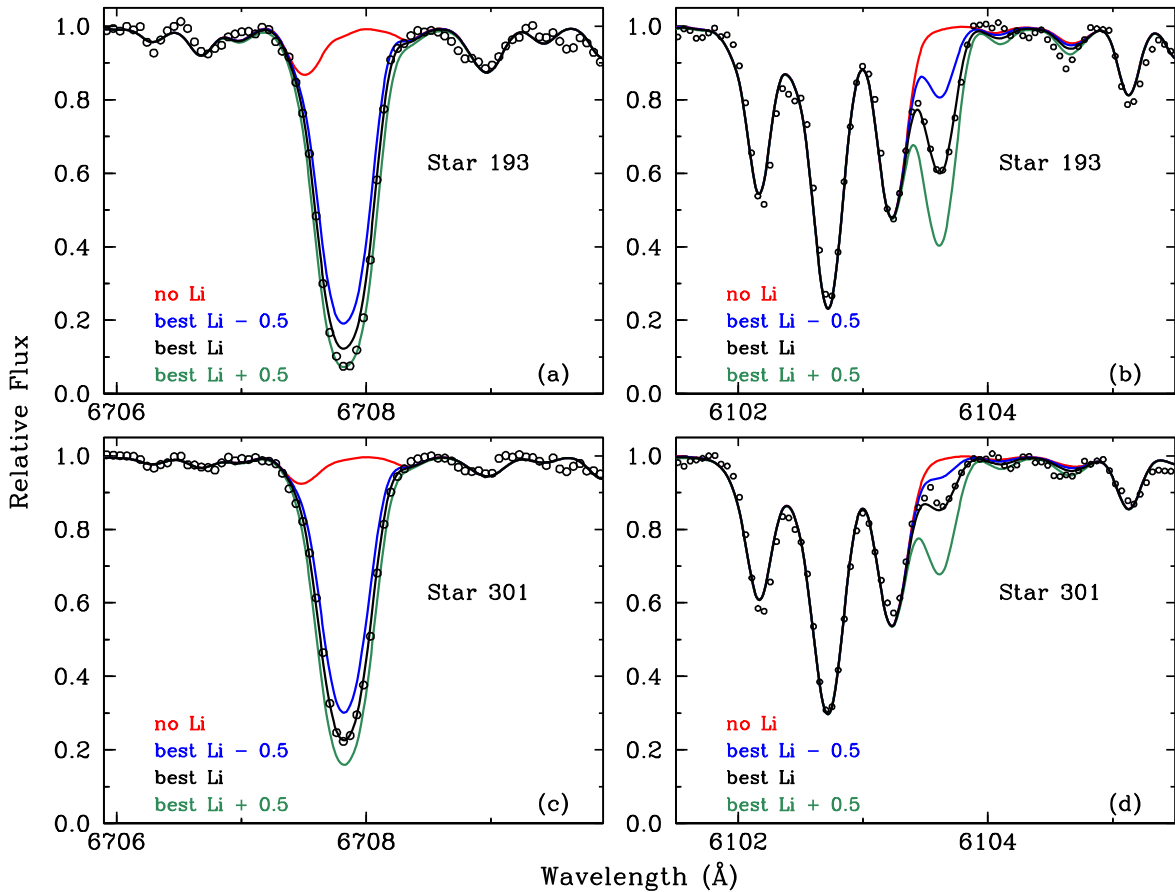

Figure 4. Observed and synthetic spectra for the two NGC 7789 stars with very high Li abundances. The λ6707 resonance lines shown in panels (a) and (c) are so saturated that they cannot yield reliable abundances. The weaker, higher-excitation λ6103 lines in panels (b) and (d) are better Li features for these two stars. (Sneden et al. 2022). In the legend of each panel, "best" indicates the synthesis using the abundance derived for the named element, and "no" indicates the synthesis computed without any contribution of this element. The other syntheses have abundance offsets (in dex) as indicated in the legends.

We estimated LiCNO abundances by comparing our observed spectra with synthetic spectra computed with our model atmospheres (Table 4) and these line lists. Full molecular equilibrium calculations were performed as part of the computations. In Figure 4 we illustrate the observed/

synthetic spectrum matches for the Li I λ6707,6103 lines in the two Li-rich stars 193 and 301. Other program stars have Li abundances that are 2–3 orders of magnitude smaller than those of stars 193 and 301, rendering weak λ6707 lines (see also Figure 2) and invisible λ6103 lines.

Figure 5. Observed and synthetic spectra for the features used to determine C, N, and O abundances in star 501, a typical program star. The observed points are shown with open circles. The meanings of the legends in each panel are the same as in Figure 4.

Table 6
LICNO Abundances, Carbon Isotopic Ratios, He EWs

Star	$^{12}C/^{13}C$	[Fe/H]	[C/Fe]	[N/Fe]	[O/Fe]	[C/N]	$\log \epsilon$(Li)	EW(He)[a]
72	15	0.01	0.09	0.29	0.22	−0.20	1.15	95
193	16	−0.02	0.12	0.12	0.07	0.00	3.50	143
301	12	−0.07	−0.10	0.27	0.07	−0.37	3.00	1040
225	⋯	⋯	⋯	⋯	⋯	⋯	⋯	102
329	35	−0.04	−0.01	0.39	0.14	−0.40	1.20	98
353	40	−0.13	0.03	0.38	0.18	−0.35	0.80	102
461	18	−0.01	0.01	0.41	0.21	−0.40	1.10	129
468	16	−0.06	0.11	0.51	0.36	−0.40	0.80	⋯
494	⋯	0.02	0.16	0.23	0.28	−0.07	1.05	39
501	22	0.00	−0.03	0.55	0.05	−0.58	1.15	145
637	25	−0.06	0.03	0.31	0.11	−0.28	1.20	110
669	22	−0.03	−0.07	0.28	0.08	−0.35	1.10	⋯
765	15	0.06	−0.06	0.34	0.09	−0.40	≲0.0	⋯
970	12	−0.02	0.00	0.47	0.17	−0.47	1.10	⋯
1066	30	−0.03	−0.12	0.38	0.03	−0.50	1.20	⋯
1101	15	−0.08	0.08	0.33	0.08	−0.25	≲0.5	⋯
< >	21	−0.03	0.02	0.35	0.14	−0.33		
σ	9	0.05	0.10	0.11	0.10	−0.16		

Note.
[a] Taken from Paper I.

For C and O, the formation of CO molecules can significantly modify the C_2 and O I number densities, so we derived these abundances iteratively. In Figure 5 we show the observed/synthetic matches for NGC 7789 star 501. Note that

although the C_2 band near 5635 Å is always weak, it is very sensitive to carbon abundance changes because of its double-carbon molecular structure (see panel (a) of Figure 5). Second, we repeat the caution from above that while the [O I] transition

Table 7
Abundance Dependencies on Model Atmosphere Parameters

Quantity	$\Delta(\log \epsilon)$	$\Delta(\log \epsilon)$	$\Delta(\log \epsilon)$	$\Delta(\log \epsilon)$
parameter	$\Delta T_{\rm eff}$	$\Delta \log g$	$\Delta [{\rm M/H}]$	$\Delta V_{\rm mic}$
change	+100 K	+0.2	+0.3	-0.2 km s^{-1}
Fe I	0.02	0.02	0.06	0.10
Fe II	-0.14	0.16	0.13	0.04
Na I	0.07	-0.02	0.01	0.08
Mg I	0.02	-0.03	0.03	0.05
Al I	0.06	-0.01	-0.02	0.06
Si I	-0.06	0.06	0.07	0.04
Ca I	0.10	-0.06	0.01	0.19
Sc II	-0.03	0.11	0.10	0.13
Ti I	0.14	0.00	-0.01	0.10
Ti II	-0.04	0.11	0.10	0.11
V I	0.17	0.10	0.00	0.20
Cr I	0.11	-0.01	0.01	0.09
Cr II	-0.09	0.11	0.09	0.06
Mn I	0.08	-0.08	0.09	0.11
Ni I	0.12	0.06	0.08	0.13
La II	0.01	0.11	0.10	0.15
Eu II	-0.01	0.12	0.10	0.15
Li I	0.15	0.00	0.00	0.00
C$_2$	-0.02	0.05	0.05	0.00
CN	-0.03	0.15	0.15	0.05
[O I]	0.02	0.13	0.12	0.01

at 6300.3 Å is the only reliable oxygen abundance indicator in optical spectra of red giant stars, it has significant blending by other lines (panel (b) of Figure 5), and results from it should be treated with caution. Finally, there are many ^{12}CN features in the $\lambda8000$ region, making total nitrogen abundance derivation straightforward. However, in all of our NGC 7789 red giants the ^{13}CN lines are much weaker (Figure 5 panel (c)), and (like many other studies) we are forced to estimate ^{12}C/^{13}C ratios mostly from the blended ^{13}CN feature at 8004.5 Å. Our derived LiCNO abundances are listed in Table 6.

3.3. Abundance Uncertainties

Our abundances depend directly on uncertainties in EW measurements and in synthetic/observed spectrum comparisons. To assess EW uncertainties we repeated EW and synthetic spectrum computations for multiple lines, varying line parameters, and continuum placement. We concluded that typical measurement uncertainties are $\pm5\%$, contributing $\sim \pm0.03$ dex to the abundances of individual spectroscopic features. The abundances also depend on the model atmosphere parameter choices. Earlier in Section 3.1 we discussed the particular analytical problem of NGC 7789 red giants. All of our program stars have strong-lined spectra, and the majority of our measured transitions are on or near the flat part of the curve of growth, where derived abundances become sensitive to assumed/derived microturbulent velocity $V_{\rm mic}$. The difficulties involved in using strong lines for model parameter derivation should be kept in mind. In Table 7 we list the responses of each species abundance to changes in model parameters that cover the range of expected uncertainties in $T_{\rm eff}$, logg, [M/H], and $V_{\rm mic}$. For this table we have chosen star 765, whose parameters are roughly in the middle of our stellar sample: $T_{\rm eff} = 4515$ K, $\log g = 2.3$, [M/H] $= -0.1$, $V_{\rm mic} = 1.4$ km s^{-1}. We present changes in abundances [X/H] (equivalent to changes in $\log \epsilon$) to show how each species responds to model parameter

changes. Lines of neutral species yield higher elemental abundances from $T_{\rm eff}$ increases due to larger ionization, and abundances from lines of ionized species increase with increasing $\log g$ due to decreased ionization in higher-gravity stars. Note that V I abundances make the largest changes as $T_{\rm eff}$ varies; this is why the LDR method works very well for $T_{\rm eff}$ estimation for our cool giant stars. Additionally, the Li abundance sensitivity to $T_{\rm eff}$ and no other atmospheric parameter in Table 7 confirms what has been known in the literature about this species for decades. Finally, in general the changes in [X/Fe] will be smaller than those of [X/H] when comparisons of neutral to neutral and ion to ion are performed as has been done in this paper.

4. Discussion

In this section, we discuss our main observational results on the light elements in NGC 7789 red giants, and consider their relationships to their probable evolutionary states.

4.1. Li and CNO Abundances

These elements are participants in the various $p - p$ and CNO cycles of hydrogen fusion, and we will consider them as a group. In Figure 6 we plot the derived ^{12}C/^{13}C and CNO abundance ratios as functions of the Li abundances. Inspection of Figure 6, as well as the mean values listed in Table 6 suggest that there are few indications of significant star-to-star CNO variations, and little evidence of their correlations with Li. For the CNO elements the abundance scatter is $\sigma \simeq 0.1$, suggesting that all of our program stars have had similar abundance changes in the first dredge up near the base of the red giant branch (RGB). Our derived C abundances in NGC 7789 do not appear to be much depleted, $\langle[{\rm C/Fe}]\rangle = 0.01$. In contrast, the classic studies of thin disk population giants derived lower C abundances. For example, Lambert & Ries (1981) found $\langle[{\rm C/Fe}]\rangle = -0.24 \pm 0.13$. We suspect that the difference stems from our exclusive use of the C$_2$ $\lambda5635$ bandhead for C abundances. Our previous study of NGC 6940 (Böcek Topcu et al. 2016) found that the $\lambda5635$ bandhead yields C abundances on average 0.17 dex higher than those derived from the much stronger $\lambda5165$ bandhead. As stated above, our spectra are not trustworthy in wavelength regions less than about 5300 Å. However, if we were to shift our derived [C/Fe] abundance ratios downward by $\simeq0.15$, then in consequence our CN-based N abundances would increase by the same amount, from $\langle[{\rm N/Fe}]\rangle = 0.35$ (Table 6) to ~0.50, compared with the Lambert & Ries value of $\langle[{\rm N/Fe}]\rangle = 0.38 \pm 0.11$. Thus we regard our C and N abundances as probably consistent with first dredge-up expectations.

Our carbon isotopic ratios are in the range ^{12}C/^{13}C = 12-40, with $\langle^{12}$C/^{13}C$\rangle = 21$ ($\sigma = 9$), again consistent with values that have been reported for field thin disk giants for decades (e.g., Tomkin et al. 1976 and references therein).

Most stars in our sample have similar Li abundances. From Table 6, excluding stars 193, 301 and 765, $\langle\log \epsilon({\rm Li})\rangle = 1.08 \pm 0.04$ (σ 0.15). This value is shared by 11 of our 14 program stars. If stars 353 and 468 with slightly smaller Li abundances ($\log \epsilon({\rm Li}) = 0.8$) are excluded the average becomes more uniform but does not change much: $\langle\log \epsilon({\rm Li})\rangle = 1.14 \pm 0.02$ (σ 0.05). In total, the Li and CNO abundances of these stars probably result from standard first dredge-up episodes that acted on a set of normal stars of similar masses
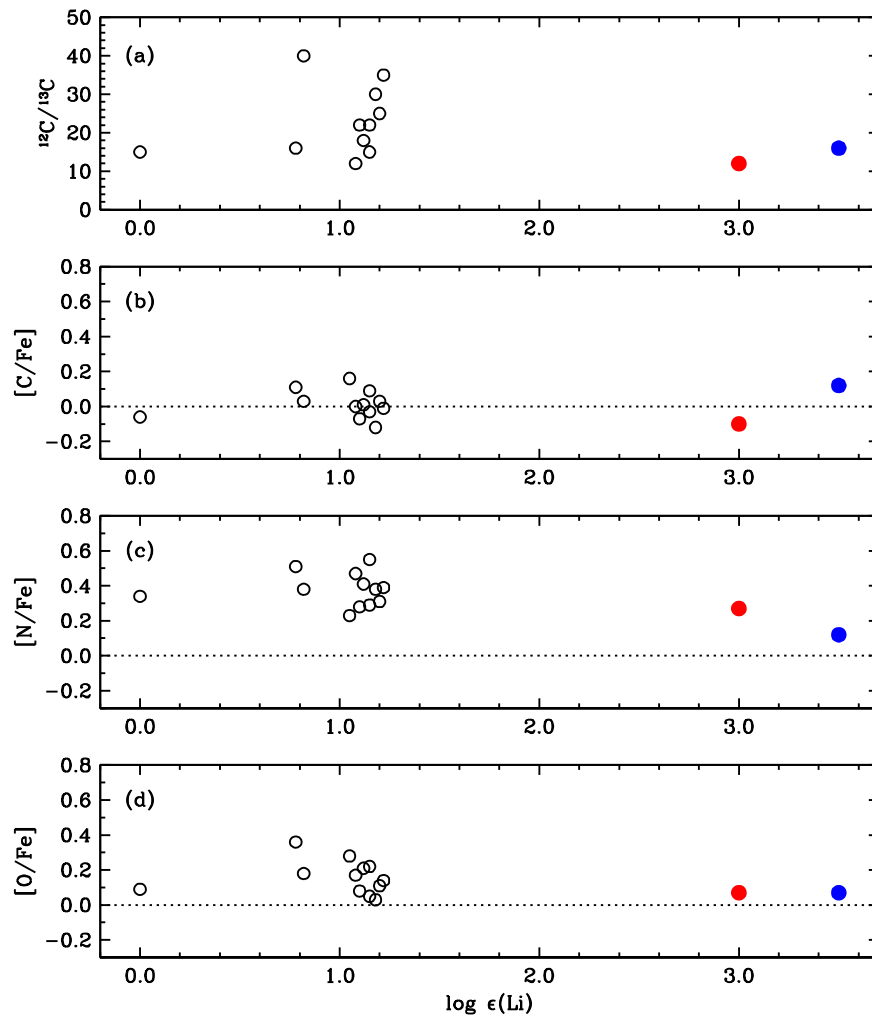
Figure 6. Carbon isotopic ratios (panel (a)) and CNO abundances (panels (b)–(d)) as functions of Li abundance in all NGC 7789 program stars, including star 193, which is a probable nonmember of the cluster. The dotted lines in panels ((b)–(d)) indicate the solar abundance values. Star 193 is the blue dot and Star 301 is the red dot.
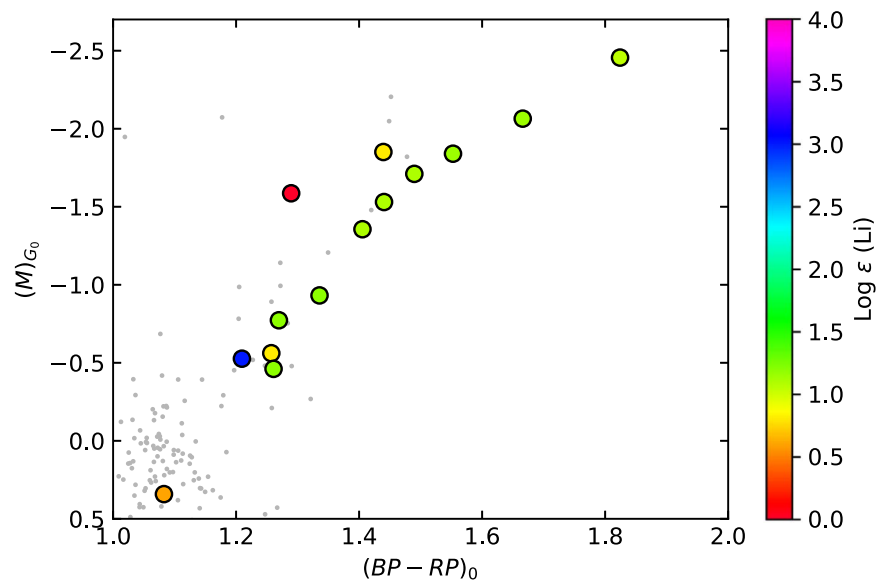

Figure 7. Another CMD for NGC 7789 with the data from Figure 1, using colors to indicate the Li abundances for NGC 7789 members.
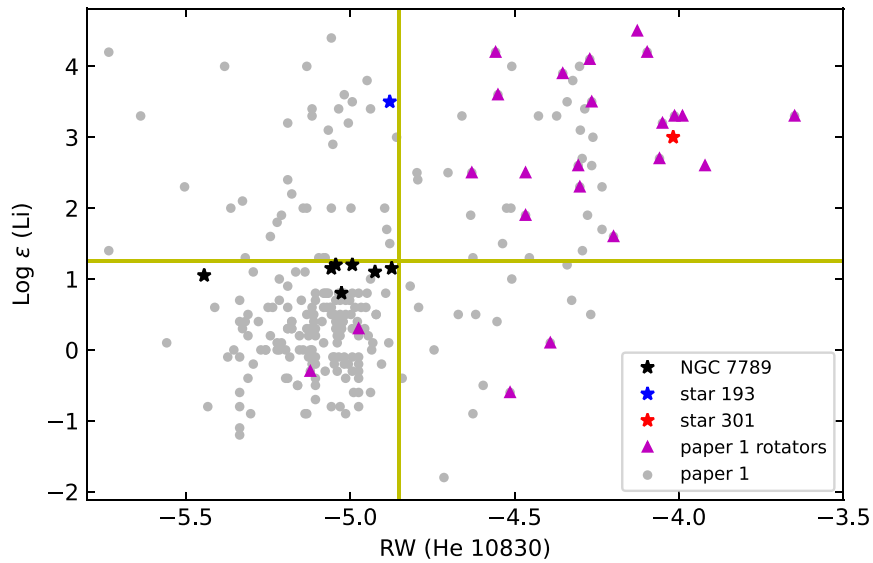
Figure 8. Correlation between lithium abundances and He absorption line strengths in Paper I and the present work. Identification of the points are in the figure legend.

and initial chemical compositions. Accurate mass measurements for individual stars would be welcome but would require astroseismology.

To help clarify the evolutionary states of our stars, in Figure 7 we repeat Figure 1 except that different colors are used to indicate derived lithium abundances. For the present purpose we do not plot star 193, the probable nonmember of NGC 7789. We suggest that all stars with $\log \epsilon(Li) \sim 1$ are first-ascent RGB members. Star 468 [$(BP - RP)_0, M_{G0}$] = [1.44, −1.85] is slightly brighter than the first-ascent sequence and might be an asymptotic giant branch (AGB) star, but the separation is small. A more convincing AGB assertion can be made for star 765 ([1.29, −1.59]), which is nearly a magnitude brighter than RGB stars with similar colors, and its Li abundance $\log \epsilon(Li) = 0.0$ is much smaller than any other program star. Star 1101 ([1.08, 0.34]) is our sole representative of the clump in NGC 7789, and being a clump star means it has evolved beyond the first-ascent RGB.

Stars 193 (not plotted in Figure 7) and 301 (the blue point in the figure) may or may not require separate interpretations. Although we agree with previous work suggesting that star 193 is not a member of NGC 7789, that fact may have little impact on the interpretation of its light element abundances. Stars 193 and 301 are solar-metallicity K giants with similar very high Li abundances. It is likely that both of them underwent similar evolutionary events that resulted in their very high surface Li contents. Star 193 departs from NGC 7789 cluster giants mainly in its relatively low [N/Fe] and consequently large [C/N] (Table 6). Ejection of star 193 from NGC 7789 membership simply puts it in good company with the many field red giants of Paper 1 that have enhanced Li while showing no evidence for chromospheric activity anomalies.

4.2. Comparison with Helium

Paper 1 reported He I $\lambda 10830$ EWs for 10 NGC 7789 red giants (see Table 6). Five of the present program stars were not observed for Paper 1, and star 225 was included in Paper 1 but not included in our optical survey. In Figure 8 we plot Li abundances versus He I reduced widths $\log(RW_{He})$.[11] We

highlight the NGC 7789 stars and add in the field stars from Paper 1 for comparison. Following the discussion in Paper 1, a yellow horizontal line is placed at $\log \epsilon(Li) = 1.25$ to approximately separate Li-rich giants from the majority of normal Li-poor stars. A vertical line set at $\log(RW_{He}) = -4.85$ provides a suggested separation between the vast majority of stars with weak He I $\lambda 10830$ absorption and the relatively few with anomalously strong He lines. These lines are rough guides and their values should not be interpreted rigidly.

In Figure 8 all program stars with $\log \epsilon(Li) \leqslant 1.15$ have weak $\lambda 10830$ absorption lines, as do the vast majority of field red giants. Probable nonmember star 193 has a large Li abundance without excess He absorption, but many other field stars share this characteristic. Member star 301 has both a high Li and a large $\lambda 10830$ feature. In fact, this star has one of the largest He I lines found in the Paper 1 survey. All other stars with $\log(RW_{He}) \gtrsim -4.2$ exhibit significant rotation spectral line broadening, with derived velocities in the range $V\sin(i) = 9$ −140 km s^{-1}. Paper 1 did not report rotational line broadening for star 301 but the derived Gaussian smoothing was larger than for most stars. Therefore we have carefully reexamined its $\lambda 10830$ region with synthetic spectra. We now tentatively can assign a small rotational value $V\sin(i) = 6 \pm 1$ km s^{-1} for star 301. However, this velocity broadening is nearly at the limit of our ability to isolate rotation from the other broadening sources (thermal, microturbulent, macrotrubulent, and instrumental), so caution should be exercised in interpretation of this value. What is not in dispute is the relatively small total line broadening of star 301 in comparison to many other Li-rich red giants.

The vast majority of the 300-star field red giant sample in Paper 1 proved to be mostly stars with colors and magnitudes consistent with the red clump and general red horizontal branch. Stars with large Li abundances and He I $\lambda 10830$ line strengths both weak and strong were as likely to occupy this CMD domain as those with neither Li nor He anomalies. The interpretation in Paper 1 centered on assignment of fresh Li production to the helium flash that preceded appearance of the stars on the red horizontal branch, as outlined in Section 1 (see also Mallick et al. 2023). This idea may be applicable for stars 301 and 193 as well. Star 301 has high Li and its strong

---
[11] $\log(RW_{He}) \equiv \log_{10}(EW_{He}/\lambda) = \log_{10}(EW_{He}/10830)$.

$\lambda10830$ line argue for recent helium-flash disturbance of its outer envelope.

However, star 301's evolutionary state is still uncertain. Based on its CMD position, certain possibilities arise. Star 301 could be ascending the RGB, in which case it would not have undergone any helium flash yet, and so both Li and He features would likely be due to interactions with a binary companion. We did not detect any binary companion in star 301's spectrum. In this case, this star's apparent excess rotation suggests that it could have an unseen companion like a white dwarf or small main-sequence star that is simply too dim to contribute any significant flux or spectral features. Figure 8 of Casey et al. (2019) presents three models for how the presence of a binary companion(s) like star(s) or planet(s) can explain the lithium richness of certain red giant stars. If star 301 is still ascending the RGB then tidal interactions with the putative companion are to blame. A radial velocity monitoring program might be useful for detecting the companion. More directly, speculation on star 301's "late" arrival on the RGB probably requires it to have recently evolved from its previous status as a cluster BSS. But such a scenario must account for star 301's carbon istopic ratio, which is among the smallest of any star in our sample (Table 6). Blame for its small ^{12}C/^{13}C would shift to the companion's transferred material.

Star 301 might be a normal red clump giant, even though its absolute magnitude (M_{G0}) appears to be ~0.5 mag brighter than the NGC 7789 clump (Figure 7). No reasonable amount of (unproven) differential reddening corrections would place star 301 in the NGC 7789 clump (see the reddening vector in Figure 1). Finally, NGC 7789 may have a more complex member population than most open clusters. From investigation of CN and CH molecular band strengths of NGC 7789 giant stars, Carrera & Martínez-Vázquez (2013) suggested that this cluster may have a CN intracluster spread of the sort seen in typical globular clusters. They urged caution in interpretation of their observations pending a much larger CN survey, but it is possible the star 301 is a representative of an anomalous subpopulation of NGC 7789. If this is true, then star 301 should be dealt with as a special evolutionary case. Asteroseismological data for this star would help its interpretation.

Star 193 has an absolute magnitude more consistent with a red clump star but it appears to be too red (Figure 1). This could be alleviated by assignments of a larger reddening value for this star than what we have assumed for the cluster. Though star 193 is a helium flash candidate, its lithium could too be explained by a binary companion as one of the binary companion models in Casey et al. (2019) involve lithium richness in post-he-flash stars but due to a binary companion rather than the helium flash.

Further progress in this area requires increasing the number of Li-rich red giants that have He I $\lambda10830$ data and other common characteristics. Efforts by our group are underway to gather such observations for Kepler field giants, whose evolutionary states can be clearly defined through asteroseismology. We are also collecting spectra of red giants with known rotational velocities to test that possible connection. Additionally the number of Li-rich red giant members in other open clusters is slowly growing (Magrini et al. 2021 and references therein). Observational campaigns on these clusters should be undertaken in the future.

5. Conclusions

In this paper we have described the derivation of model atmospheric parameters and LiCNO abundances for 15 red giants of the open cluster NGC 7789. We have explored the relationship between Li abundances, CNO abundances, and He $\lambda10830$ absorption strengths. We find that the majority of observed NGC 7789 stars have consistent Li abundances, $\log \epsilon(\mathrm{Li}) \simeq 1.0$. Two anomalous stars 193 and 301 have $\log \epsilon(\mathrm{Li})$ of 3.5 and 3.0, respectively; they are unambiguous examples of the Li-rich red giant subclass. The probable nonmembership of star 193 hinders a detailed investigation of its evolutionary state, but its Li abundance is well determined. The He I $\lambda10830$ transition does not lead to an easy interpretation of the Li richness of stars 193 and 301, given the feature is present in one star but not the other. In concert with other papers on Li abundance enhancements in field red giants, we suggest (but cannot prove) that the Li and He peculiarities detected in a small percentage of giants are due to recent or long-ago envelope turbulence that accompanied the helium flashes in these stars. Li abundances and He line strength measurements for many other NGC 7789 red giants should go a long way to clarifying the overall stellar evolution story of this cluster.

ORCID iDs

Neel Nagarajan ⓘ https://orcid.org/0000-0002-7112-2086
Christopher Sneden ⓘ https://orcid.org/0000-0002-3456-5929
Melike Afşar ⓘ https://orcid.org/0000-0002-2516-1949
Catherine A. Pilachowski ⓘ https://orcid.org/0000-0002-3007-206X

References

Alexander, J. B. 1967, Obs, 87, 238
Anthony-Twarog, B. J., Deliyannis, C. P., Rich, E., & Twarog, B. A. 2013, ApJL, 767, L19
Biazzo, K., Frasca, A., Catalano, S., & Marilli, E. 2007, AN, 328, 938
Böcek Topcu, G., Afşar, M., Schaeuble, M., & Sneden, C. 2015, MNRAS, 446, 3562
Böcek Topcu, G., Afşar, M., & Sneden, C. 2016, MNRAS, 463, 580
Brooke, J. S. A., Bernath, P. F., Western, C. M., et al. 2016, JQSRT, 168, 142
Burbidge, E. M., & Sandage, A. 1958, ApJ, 128, 174
Cameron, A. G. W., & Fowler, W. A. 1971, ApJ, 164, 111
Cantat-Gaudin, T., Jordi, C., Vallenari, A., et al. 2018, A&A, 618, A93
Carlberg, J. K., Cunha, K., & Smith, V. V. 2016, ApJ, 827, 129

Carrera, R., & Martínez-Vázquez, C. E. 2013, A&A, 560, A5
Casey, A. R., Ho, A. Y. Q., Ness, M., et al. 2019, ApJ, 880, 125
Deepak, R. B. E., & Reddy, B. E. 2019, MNRAS, 484, 2000
Den Hartog, E. A., Lawler, J. E., Sneden, C., et al. 2021, ApJS, 255, 27
Fitzpatrick, M. J., & Sneden, C. 1987, BAAS, 19, 1129
Gaia Collaboration, Prusti, T., de Bruijne, J. H. J., et al. 2016, A&A, 595, A1
Gaia Collaboration, Schultheis, M., Zhao, H., et al. 2022, arXiv:2206.05536
Gaia Collaboration, Vallenari, A., Brown, A. G. A., et al. 2022, arXiv:2208.00211
Gao, X.-h. 2018, PASP, 130, 124101
Gim, M., Vandenberg, D. A., Stetson, P. B., Hesser, J. E., & Zurek, D. R. 1998, PASP, 110, 1318
Gray, D. F. 2008, The Observation and Analysis of Stellar Photospheres (Cambridge: Cambridge Univ. Press)
Gray, D. F., & Johanson, H. L. 1991, PASP, 103, 439
Hills, J. G., & Day, C. A. 1976, ApL, 17, 87
Jacobson, H. R., Pilachowski, C. A., & Friel, E. D. 2011, AJ, 142, 59
Jordi, C., Gebran, M., Carrasco, J. M., et al. 2010, A&A, 523, A48
Kurucz, R. L. 2011, CaJPh, 89, 417
Kurucz, R. L. 2018, in ASP Conf. Ser. 515, Workshop on Astrophysical Opacities, ed. C. Mendoza, S. Turck-Chiéze, & J. Colgan (San Francisco, CA: ASP), 47
Küstner, F. 1923, VeBon, 18, 1
Lambert, D. L., & Ries, L. M. 1981, ApJ, 248, 228
López-Valdivia, R., Mace, G. N., Sokal, K. R., et al. 2019, ApJ, 879, 105

Magrini, L., Smiljanic, R., Franciosini, E., et al. 2021, A&A, 655, A23
Mallick, A., Singh, R., & Reddy, B. E. 2023, ApJL, 944, L5
Martell, S. L., Simpson, J. D., Balasubramaniam, A. G., et al. 2021, MNRAS, 505, 5340
McCrea, W. H. 1964, MNRAS, 128, 147
Overbeek, J. C., Friel, E. D., Jacobson, H. R., et al. 2015, AJ, 149, 15
Pancino, E., Carrera, R., Rossetti, E., & Gallart, C. 2010, A&A, 511, A56
Perets, H. B., & Fabrycky, D. C. 2009, ApJ, 697, 1048
Pilachowski, C. 1986, ApJ, 300, 289
Placco, V. M., Sneden, C., Roederer, I. U., et al. 2021, linemake: Line list generator, Astrophysics Source Code Library, ascl:2104.027
Sandquist, E. L., Stello, D., Arentoft, T., et al. 2020, AJ, 159, 96
Sneden, C. 1973, ApJ, 184, 839
Sneden, C., Afşar, M., Bozkurt, Z., et al. 2022, ApJ, 940, 12
Strassmeier, K. G., & Schordan, P. 2000, AN, 321, 277
Sun, Q., Deliyannis, C. P., Twarog, B. A., et al. 2022, MNRAS, 513, 5387
Tautvaišienė, G., Edvardsson, B., Puzeras, E., & Ilyin, I. 2005, A&A, 431, 933
Tody, D. 1986, Proc. SPIE, 627, 733
Tody, D. 1993, in ASP Conf. Ser. 52, Astronomical Data Analysis Software and Systems II, ed. R. J. Hanisch, R. J. V. Brissenden, & J. Barnes (San Francisco, CA: ASP), 173
Tomkin, J., Luck, R. E., & Lambert, D. L. 1976, ApJ, 210, 694
Tull, R. G., MacQueen, P. J., Sneden, C., & Lambert, D. L. 1995, PASP, 107, 251
Wallerstein, G., & Helfer, H. L. 1959, ApJ, 129, 720